ADVANCED FUNCTIONAL MATERIALS
www.afm-journal.de

Towards Low Cost and Sustainable Thin Film Thermoelectric Devices Based on Quaternary Chalcogenides

*Eleonora Isotta, Jacob Andrade-Arvizu, Ubaidah Syafiq, Alex Jiménez-Arguijo, Alejandro Navarro-Güell, Maxim Guc, Edgardo Saucedo, and Paolo Scardi**

A major challenge in thermoelectrics (TEs) is developing devices made of sustainable, abundant, and non-toxic materials. Furthermore, the technological drive toward low sizes makes crucial the study of nano and micro configurations. In this work, thin film TE devices based on p-type $Cu_{2+x}Zn_{1-x}SnS_4$ and $Cu_{2+x}Zn_{1-x}SnSe_4$, and n-type $Al_yZn_{1-y}O$ are fabricated by physical vapor deposition. The kesterite phases show good purity and promising TE power factor, likely enhanced by the copper–zinc order–disorder transition. Thin film generators in planar configuration are assembled by a sequential deposition of the p-type, n-type, and contact materials. The power per unit planar area reaches 153 and 279 nW cm^{-2} for the sulphur- and selenium-based generators, respectively. These values significantly outperform any other literature attempt based on sustainable and low-cost thin films. Furthermore, if compared with traditional TEs often made of scarce and toxic materials, these devices offer a cost reduction above 80%. This allows reaching comparable values of power density per unit material cost, representing a first real step toward the development of sustainable and non-toxic thin film TE devices. These can find applications in micro energy harvesters, microelectronics coolers, and temperature controllers for wearables, medical appliances, and sensors for the internet of things.

1. Introduction

Thermoelectric (TE) energy conversion is deemed one of the most promising technologies for the recovery of waste heat, especially in the low-grade form (<500 K), and for solid state cooling.[1] It is valued for being compact, reliable, silent, and with little to no maintenance required. TE materials can generate a voltage when a temperature gradient is applied and vice versa, through the Seebeck and the Peltier effects, respectively. The TE performance of a material can be assessed by the figure of merit, $zT = S^2 T/\rho\kappa = \mathrm{PF}\, T/\kappa$, where S is the Seebeck coefficient, ρ is the electrical resistivity, κ is the thermal conductivity, T is the absolute temperature, and PF is the power factor. Much research in TEs has been dedicated to strategies to improve the materials zT. Due to the strong coupling of the TE parameters, the first step is optimizing the Fermi level yielding the optimal carrier concentration.[2–5] Further, methods are typically employed to reduce the lattice component of κ, which is independent of the carrier density, to obtain a so called phonon-glass electron-crystal material.[6] Among the most common ones are nanostructuring,[1,7,8] hierarchical architecture,[9,10] and nanoprecipitates.[11,12] Additional mechanisms that proved promising in TEs include energy filtering,[13,14] band convergence,[15,16] resonant state doping, and spin-enabled mechanisms.[17–19]

Successful strategies in materials, however, needs to be tested in real devices. For the sake of power generation, TE materials are assembled in a thermoelectric generator (TEG) typically consisting of p-type and n-type semiconductors (called legs) connected electrically in series and thermally in parallel.

Among the possible TEG configurations, thin film based devices have emerged as an attractive possibility. Indeed, since the early theoretical studies of Dresselhaus and Hicks,[20,21] low dimensional structures have been regarded amongst the

E. Isotta, U. Syafiq, P. Scardi
Department of Civil
Environmental and Mechanical Engineering
University of Trento
via Mesiano 77, 38123 Trento, Italy
E-mail: paolo.scardi@unitn.it

The ORCID identification number(s) for the author(s) of this article can be found under https://doi.org/10.1002/adfm.202202157.

DOI: 10.1002/adfm.202202157

J. Andrade-Arvizu, A. Jiménez-Arguijo, M. Guc
Solar Energy Materials and Systems Group
Catalonia Institute for Energy Research (IREC)
Jardins de les Dones de Negre 1, Sant Adrià de Besòs, 08930 Barcelona, Spain

U. Syafiq
Solar Energy Research Institute
the National University of Malaysia (SERI-UKM)
Bangi, Selangor 43600, Malaysia

A. Jiménez-Arguijo, A. Navarro-Güell, E. Saucedo
Photovoltaic Group
Electronic Engineering Department
Polytechnic University of Catalonia (UPC)
Av. D'Eduard Maristany, 16, Sant Adrià de Besòs, 08930 Barcelona, Spain

most promising strategies to decouple the TE properties and enhance the material performance.[22,23] To date, some of the highest performances have been obtained with nanostructures, like nanodots[24] and nanowires,[25,26] and thin films.[27,28] Nevertheless, the first two have not yet been translated into real applications (i.e., no available devices).

From a technical point of view, thin films bring significant advantages over bulk TEs in terms of material cost, retention of the thermal gradient, adaptability to curved and flexible substrates, as well as the possibility to realize transparent devices. Furthermore, small size and lightweight are important for easier integration in competitive applications of TEs like micro power generation, thermal regulation, micro cooling, and sensing. These TE-based devices are deemed promising add-ons for micromachines,[29] textile-integrated appliances and smart clothing,[30,31] wearables,[32] healthcare and implantable devices,[33] as well as the internet of things.[34,35] For these reasons, it turns out meaningful and convenient to develop thin film based TEGs. Organic thin-film TEs have been proposed as promising solutions[36–39] due to their potential transparency, bendability and low cost, but they are generally restricted to lower temperature applications.

Typical TE materials are made of expensive and critical raw elements like Bi, Te, Mg, and Sb,[40] or toxic compounds such as Pb. Developing TEGs based on low-cost materials[41] and with a decent performance has emerged as even more important than targeting a very-high zT.[42] Furthermore, a wide development of the TE technology in every-day life appliances requires sustainable and non-toxic materials.

In the recent literature of applied TEs there seems to be two main approaches. On the one hand, a considerable effort has been made to search new compounds with good performance, low cost and sustainable. On the other, much research has been dedicated to fabricating devices and designing novel TEG architectures, so far mostly based on traditional high-performance materials (like Bi_2Te_3 or Sb_2Te_3).[43–45] Feeble has been the effort in developing functioning devices based on alternative cost-effective materials.

In this work, we use low-cost, abundant, and sustainable p-type $Cu_{2+x}Zn_{1-x}SnS_4$ and $Cu_{2+x}Zn_{1-x}SnSe_4$ (CZTS, CZTSe), and n-type $Al_yZn_{1-y}O$ (AZO) to design and produce thin film TE devices, with amongst the highest performance in the literature. A structural and transport-property characterization of materials is presented, and TEGs prototypes with promising performance are shown. We believe this to be an important step toward the realization of efficient thin film TE devices, based on low-cost and sustainable materials, as well as the first attempt of developing kesterite-based TE energy generators.

2. Experimental Section

2.1. Thin Film Preparation

Thin film samples, with targeted nominal stoichiometry $Cu_{2.125}Zn_{0.875}SnS_4$ (CZTS) and $Cu_{2.125}Zn_{0.875}SnSe_4$ (CZTSe) were fabricated through a sequential process. First, a Cu/Sn/Cu/Zn metallic precursor stack using 99.99% purity targets was deposited by direct current (DC) magnetron sputtering (Alliance Concept AC450) onto 1 mm thickness soda-lime glass (SLG) supporting substrates. The sputtering conditions in the chamber mainly consisted in an Ar plasma pressurized at $\approx 3 \times 10^{-3}$ mbar by 50 W for Sn, and 100 W for the Cu and Zn targets. The thickness of the different layers of the stack was selected to target a Cu-rich composition with nominal values of [Cu]/([Zn] + [Sn]) = 1.133 and [Zn]/[Sn] = 0.875. For the chalcogenization step, the metallic precursors were introduced into a graphite box of 69 cm^3 inside a three-zone tubular furnace with S or Se+Sn atmosphere (100 mg of S (Alfa-Aesar pieces, random sizes, 99.999%) or Se (Alfa-Aesar powder, 200 mesh, 99.999%) and 5 mg of Sn (Alfa-Aesar powder, 100 mesh, 99.995%). The chalcogenization thermal profiles and conditions have been optimized for the growth of kesterite thin film for photovoltaic applications, as previously described in refs. [46–49]. An illustration of the thermal profiles is presented in the Supporting Information.

Thin film samples of Al-doped ZnO (AZO) were deposited via radio frequency (RF) magnetron sputtering (Leybold-Heraeus LH Z400 MS) on SLG substrates with 1 mm thickness. An AZO target with 98% ZnO and 2% Al_2O_3 was used as sputtering source, with a power of 50 W, frequency 13.6 MHz, and a 31% Ar atmosphere with a minimum working pressure of $\approx 5 \times 10^{-6}$ mbar. A sputtering time of 10 min was selected to achieve thicknesses in the order of 250 nm.

2.2. Structural, Chemical, and Morphological Characterization

X-ray diffraction (XRD) patterns were collected in pseudo-parallel beam geometry with a Bruker D8 Discover (Karlsruhe, Germany) diffractometer, with Co-Kα radiation operated at 35 kV and 40 mA.

A Rietveld refinement of XRD data was performed with the software TOPAS 7,[27] with the aid of whole powder pattern modelling[28] (WPPM) macros[29] for the analysis of crystal domain size and strain.

Raman scattering measurements were performed using special probes designed at the Catalonia Institute for Energy Research (IREC) connected to FHR-640 monochromator coupled with deep cooled CCD detector. The spectra were measured in backscattering configuration using a He–Cd gas laser (325 nm, $\approx$60 W cm^{-2}) and a solid-state laser (532 nm, $\approx$100 W cm^{-2}) as excitation sources. The first laser was used for the AZO thin film characterization and the second for the kesterite thin films analysis. The spectra were calibrated by imposing the position of the main peak of monocrystalline Si to 520 cm^{-1}.

UV–vis spectroscopy was performed with two PerkinElmer spectrophotometers, a Lambda 750 and a Lambda 950, equipped with a 150 mm integrating sphere and a spectral response analysis system (Bentham PVE300) calibrated by an Si and a Ge photodiode. Optical absorption spectra were collected in the wavelength range 300–1000 nm, with a 0.5 nm step size. Tauc's plots were used to estimate the bandgap values.

The chemical composition was confirmed with energy dispersive X-ray spectroscopy (EDXS), performed with a Coxem EM-30AX instrument operated at 20 kV electron beam accelerating voltage, spot size of 16 and current in the order of 47 μA. Surface and fracture surface morphology was observed with

scanning electron microscopy (SEM) imaging with a JEOL IT300 Instrument (Japan), operated at 20 kV electron beam accelerating voltage.

A Dektak 3 surface profilometer with a 2.5 μm radius diamond-tip stylus was used to measure the film thicknesses, with a 2 mm scan range perpendicular to a linear notch scratched on the film.

2.3. Thermoelectric Characterization

In-plane measurements of Seebeck coefficient and electrical resistivity were performed on a Linseis LSR-3 machine, adapted to host thin films. Schematics and pictures of the setup are in Supporting Information. Samples with a rectangular geometry of approximately 15 mm × 5 mm were mounted on the setup with the aid of a thin film adaptor. Electrical resistivity was measured in 2-contact configuration, while the absolute Seebeck coefficient was measured in 4-contact configuration with Pt standard and a temperature gradient of ≈10 °C. As a further confirmation, electrical resistivity values were checked with a Signatone S-302 4-point probe connected with a Keithley 2601A multimeter. The Seebeck coefficient was checked on individual legs in the TEG setup described below.

2.4. Device Fabrication

TEG devices were fabricated in several successive steps illustrated in **Figure 1**a. First, squared SLG substrates of 1 mm thickness and approximately 25 mm lateral side were cleaned with pH-neutral soap and concentrated KOH in ethanol, rinsed with distilled water, and then dried with compressed air. Second, the p-type material was sputtered on the whole substrate area and the chalcogenization treatment was applied, as described in Section 2.1. Third, most of the p-type material was gently scratched away with a precision blade to realize the p-type legs. Fourth, a kapton-tape mask was applied on the device leaving out only the required space for the sputtering of the n-type material, using paper strips to protect the area with the p-type legs. AZO was then sputtered as described in Section 2.1. Finally, Ag contacts were deposited via thermal evaporation (Tecuum AG VCM600 V1) to connect all the legs in series. A kapton-tape mask with specific patterns for the contacts and protection paper for the legs were used during the evaporation. Whenever necessary, the Ag contacts were patched with some Ag paste to reinforce the robustness during measurements. A schematic of the end device is visible in Figure 1b. Two types of TEG configuration were studied and characterized: a "standard" configuration, consisting of two p–n couples with each leg having a width of ≈3 mm and a height of ≈15 mm, and an "optimized" configuration, composed of four p–n couples with variable width of the n and p-type legs. The width for the latter case was selected with a minimization process (described in Section 3.3), targeted to the optimization of the electrical conductance to thermal conductance ratio of the p and n legs. Furthermore, special care was paid to minimize the free (inactive) area on the substrate. A picture of the final TEG devices is presented in Figure 1c.

2.5. Device Characterization

The overall device resistance was measured with a multimeter. Open circuit voltage V_{OC} versus temperature difference ΔT plots were acquired with an in-house setup, which illustration and picture can be seen in **Figure 2**a and b, respectively. A hot plate, in contact with the bottom-lateral side of the TEG substrate, was used as heat source, while a metal plate was used as heat dissipator (no active cooling). Spring-loaded contacts were connected to the two ends of the TEG and the generated voltage was measured with a Keithley 2601A voltmeter. The hot plate temperature was varied between 50–250 °C, and 10 °C steps were used for the acquisition. The temperature difference was measured with a Fluke Ti9 thermal camera, as visible in Figure 2c. Measurements were performed in air.

Current–voltage–power *IVP* characteristics were measured with an analogue setup illustrated by the equivalent circuit in Figure 2d, using a Keithley 2601A as the voltmeter, a Hewlett Packard 34401A as the ammeter, and a variable resistor. The hotplate temperature was maintained at 250 °C for these measurements. At every temperature difference, there was a transient time in which the voltage (and current) increased, peaked, and gradually decreased following to thermal equilibration. All the specified values refer to the peak ones.

3. Results and Discussion

3.1. Structural, Optical, and Compositional Characterization of the Thin Films

Cu_2ZnSnS_4 and $Cu_2ZnSnSe_4$, also known as kesterite(s), have been widely researched in the past years as alternative sustainable materials for thin film photovoltaic (PV) applications.[50–54] They are valued for the low-cost and abundance of the constitutive elements as well as good light harvesting properties. Their p-type semiconducting nature is ascribed to the low formation energy of copper vacancies V_{Cu} and Cu_{Zn} antisite defects.[55] A few studies on the TE performance of kesterites in bulk form revealed improved properties when cation disorder is introduced,[56–59] and with Cu-doping,[60–62] especially for the selenide compound.[61,63–66] In particular, they have been deemed promising materials for their exceptional TE performance over cost ratio,[60] thus making them particularly interesting for sustainable and low cost generation. Surprisingly, it emerges a substantial scarcity of TE investigation for the thin film configuration of these materials,[67,68] despite the vast knowledge acquired in their fabrication and PV characterization.[46,69–71] Following literature guidelines on bulk counterparts,[60,66] a 12.5% Cu doped (in place of Zn) composition is selected for the thin films fabricated in this work.

Al-doped ZnO (AZO) is regarded as a good n-type TE material,[72] fully composed of sustainable, non-toxic and inexpensive elements. As a bulk material, it is limited by the large thermal conductivity κ,[73] an issue demonstrated to be attenuated when in thin film form.[74] Furthermore, thin film AZO is valued for being transparent as well as with excellent mechanical and thermal stability.[74] A 98% ZnO and 2% Al_2O_3 sputtering source is used for the realization of AZO films in this work, corresponding to

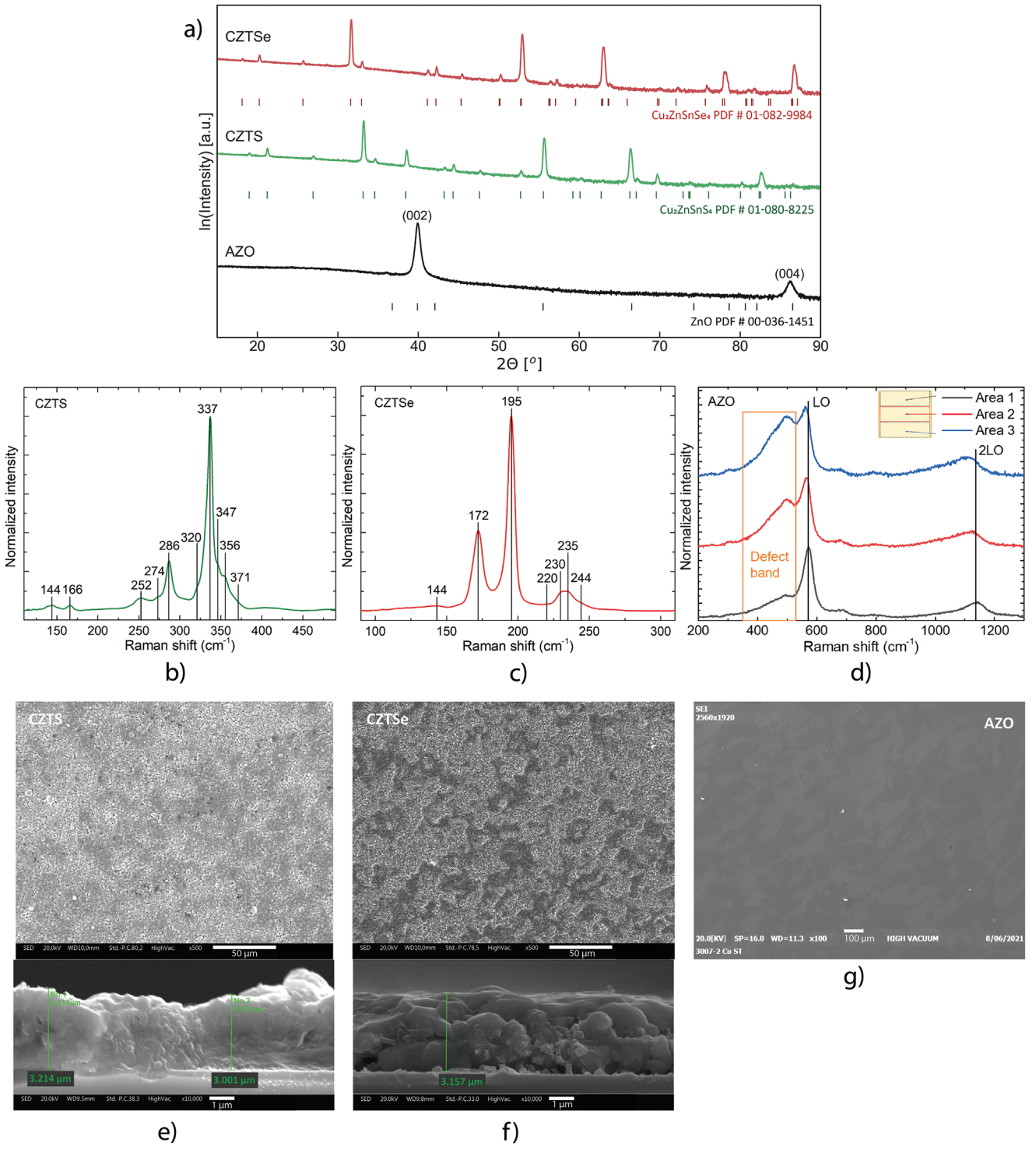

Figure 1. Structural and morphological characterization of the CZTS, CZTSe, and AZO samples. a) X-ray diffraction patterns and b,c,d) Raman spectra for a Cu-doped CZTS, Cu-doped CZTSe, and AZO samples, respectively. In (d), different regions of the AZO sample (20 mm × 20 mm of total area) were analyzed to understand the chemical variability. Scanning electron microscopy imaging for the e) CZTS and f) CZTSe samples, with in-plane and cross-sectional images, and in plane imaging for the g) AZO sample.

a nominal stoichiometry of $Al_{0.039}Zn_{0.961}O$. The choice of AZO results particularly convenient for our case as it does not require any post-treatment, allowing to deposit it aside CZTS and CZTSe in their final form (after the chalcogenization process).

First, a full characterization of the individual thin films (CZTS, CZTSe, and AZO) is performed.

X-ray diffraction (XRD) and Raman spectroscopy measurements indicate a good phase purity for all the samples, with no

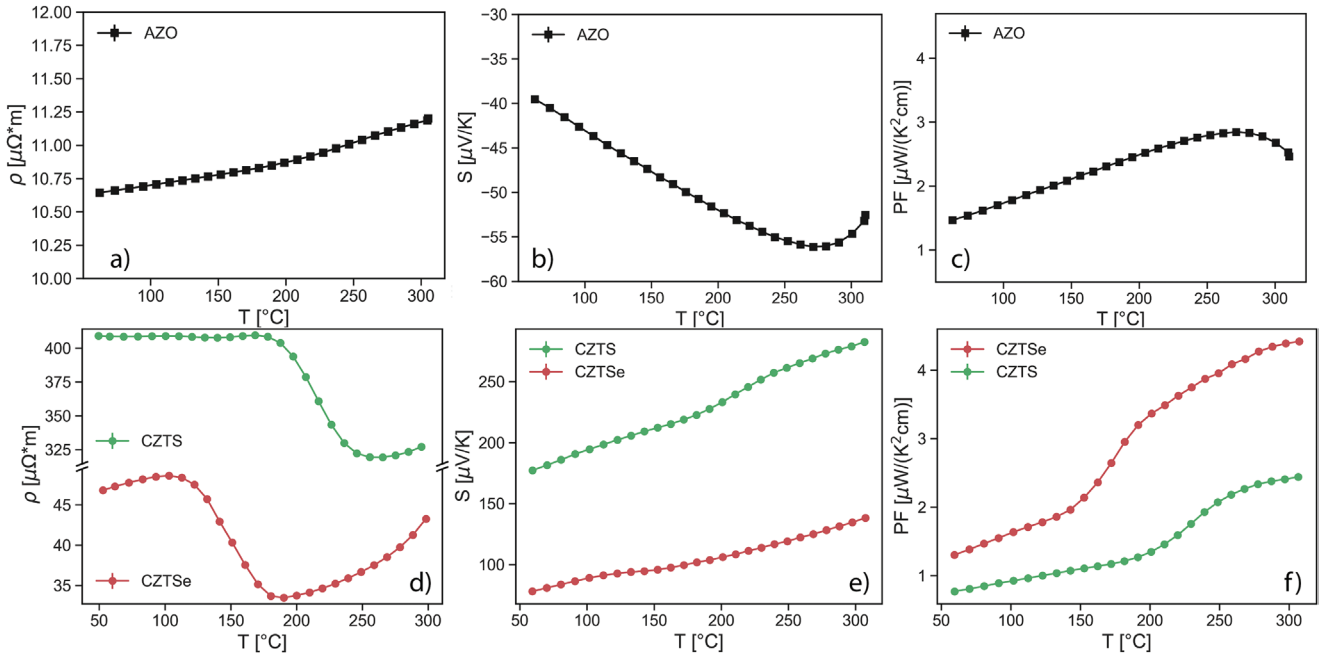

Figure 2. Thermoelectric properties of AZO, CZTS, and CZTSe thin films. a,d) The electrical resistivity ρ, b,e) Seebeck coefficient (or thermopower) S, and c,f) power factor PF were measured respectively for AZO, and CZTS, CZTSe thin film samples.

measurable trace of secondary phases. As visible in **Figure 3**a all the XRD reflections observed for the CZTS and CZTSe samples can be indexed with the respective tetragonal I-4 kesterite phases (for reference, PDF # 01-080-8225 for CZTS,[75] and 01-082-9984 for CZTSe[76]). The larger size of the anion causes the lattice parameter to be larger for CZTSe, as visible by the

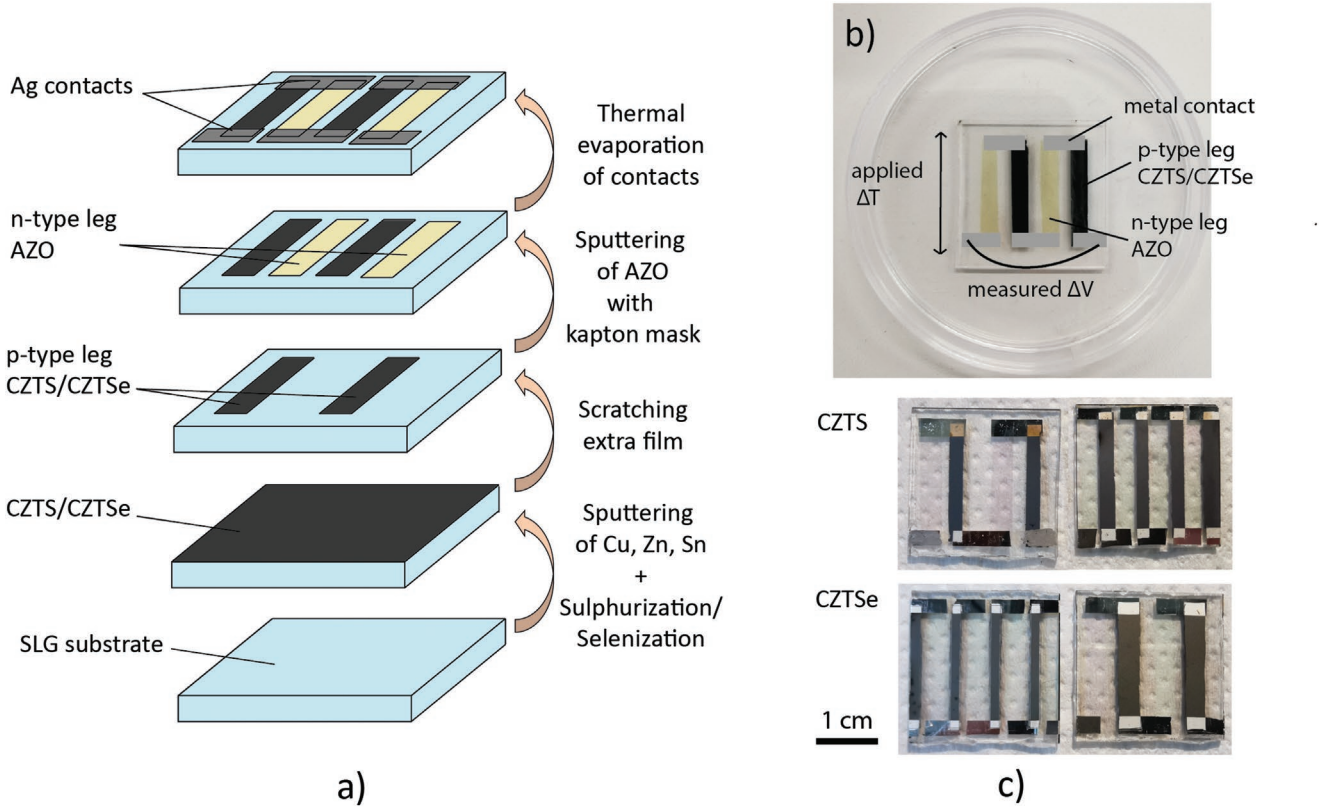

Figure 3. a) Illustration of the steps to fabricate CZTS/CZTSe and AZO TEGs. b) A scheme of the end TEG device. c) Pictures of the realized devices for both CZTS and CZTSe p-side and in standard (2 p–n couples) and optimized (4 p–n couples) configurations.

Table 1. Chemical composition of the CZTS, CZTSe, and AZO thin-film samples obtained with energy dispersive X-ray spectroscopy.

	Cu [at%]	Zn [at%]	Sn [at%]	S [at%]	Se [at%]	Cu/(Zn+Sn)	Zn/Sn
CZTS	26.3(8)	10.12(3)	13.18(8)	50(1)		1.13	0.77
CZTSe	26.7(6)	10.6(3)	13.4(6)		49(1)	1.11	0.79
	Al [at%]	Zn [at%]	O [at%]	Si [at%]	Ca [at%]	Al/Zn	
AZO	1.3(2)	36.1(2)	54.1(3)	6.6(3)	1.8(1)	0.036	

shift of reflections to lower 2θ angles. Raman scattering on as-deposited samples (Figure 3b,c) shows the typical spectra for kesterite compounds with well pronounced peaks at 286 and 337 cm^{-1} for CZTS,[77] and 172 and 195 cm^{-1} for CZTSe.[78] Peaks in the XRD patterns and Raman spectra are relatively sharp, indicating a good crystallinity for both compounds. More details from the Rietveld refinement of XRD data can be found in Supporting Information.

The XRD pattern of the AZO sample (Figure 3a) shows missing peaks with respect to the reported hexagonal $P6_3mc$ phase of ZnO (PDF # 00-036-1451[79]), with dominant (002) and second-order (004) reflections. This is an indication of strong texturing of the sample along the [00l] direction, quite expected for hexagonal phase thin films deposited by sputtering. The Raman spectra (Figure 3d) show the typical shape for Al-doped ZnO, with the most intense LO-like peak, the second order of this (2LO) and with a defect band.[80,81] The latter is assigned to phonon-plasmon interaction, and its relative intensity directly correlates with the electrical resistivity of the AZO layer.[80,81] The intensity of this band is found to vary across the sample, pointing to inhomogeneities leading to spatial changes in electrical resistivity (see further discussion in Section 3.3).

Scanning electron microscopy (SEM) imaging, in Figure 3e,f,g (and Supporting Information), shows submicrometer-size domains for CZTS and CZTSe, in accordance with the Rietveld refinement of XRD patterns (see Supporting Information). Films are observed to be compact and ≈3 µm thick, in agreement with profilometer measurements yielding thicknesses of 2.5 µm for CZTS and 3 µm for CZTSe. The AZO layer shows a compact and pin-hole free planar morphology (Figure 3g), and the profilometer thickness is measured in the order of 250 nm.

The chemical composition of the films was analyzed by energy dispersive X-ray spectroscopy (EDXS), and results can be seen in **Table 1**. The p-type samples were prepared with a nominal stoichiometry of $Cu_{2.125}Zn_{0.875}SnX_4$ (X = S, Se), as similar compositions have been shown in the literature to be favorable in terms of bulk TE properties.[60–63] This happens because the Cu_{Zn} antisite can act as an acceptor defect, thus promoting p-type carriers. Consistently, compositional results show a Cu-rich and Zn-deficient composition, with the cations ratios close to the nominal precursor composition with slightly higher Sn content. Compositional maps (in Supporting Information) show an even distribution of the elements. EDXS on the AZO thin film highlights a 3.6% excess of Al with respect to Zn, reasonably in accordance with the nominal stoichiometry. Oxygen, silicon, and calcium are detected as well, evidencing the penetration of the electron beam in the SLG substrate, as expected given the low thickness of the AZO film.

3.2. Thermoelectric Characterization of the Thin Films

The electronic properties of the thin films are reported in **Figure 4**. For the measurements, an AZO specimen was cut from the central area of the sputtered batch, shown to be less affected by compositional inhomogeneities (further discussion in Section 3.3 and Supporting Information). AZO (Figure 4a–c) shows an n-type conduction, in agreement with literature reports[82–86] and predictions based on ZnO defect formation energies.[72] The electrical resistivity ρ and Seebeck coefficient S (or thermopower) show values respectively ranging from 10.6 µΩ m and −39 µV K^{-1} at 50 °C to 11.25 µΩ m and −54 µV K^{-1} at 300 °C, from in-accordance[85,86] to lower[83,84] than most of the literature. The latter fact points to a possible high carrier concentration, in agreement with the degenerate semiconducting nature visible in the slight increase in ρ with temperature.

CZTS and CZTSe (Figure 4d–f) films show a p-type behavior. The samples display a relatively low ρ as expected for the p-type doping, with values comparable with Cu-doped bulk samples in the literature.[60,61,66,87] A reduction in ρ is noticed in the range 180–270 °C and 120–180 °C, respectively for CZTS and CZTSe. Around the same temperatures, CZTS shows a slight increase in S. We elucidate that these features can be related with Cu–Zn disorder. Indeed, both compounds are reported to face a reversible order-disorder phase transition, at 260 ± 10 °C for CZTS[88] and 200 ± 20 °C for CZTSe.[89] This features a randomization of the Cu and Zn occupancy in the intermediate 1/4 and 3/4 planes of ordered I-4 kesterite, thus transitioning to the I-42m space group or disordered kesterite structure.[90] In pristine bulk and thin film CZTS, the transition to disordered kesterite has been demonstrated to cause a sharp increase in the Seebeck coefficient, without a detrimental effect on electrical resistivity.[56,57,67] This has been shown being connected with a favorable modification in the electronic band structure, which acquires flatter and more converged bands.[57] In the CZTS sample presented here, transition features appear largely smoothed out (small kink in S rather than marked increase, see refs. [56,67]). This can be related to the compositional differences of the kesterites, which had been shown to have an impact on the disorder evolution with the thin film temperature,[91] and thus may justify less-marked features at the transition.[92]

In order to investigate possible origins at the base of the observed drop in electrical resistivity close to the transition temperature, we have measured the electronic bandgap E_g of CZTSe. Indeed, CZTSe has been reported to face a reduction in E_g of around ≈110 meV when transitioning to disordered kesterite.[89] However, we did not find any significant change in the experimental bandgap. Indeed, a sample of CZTSe was

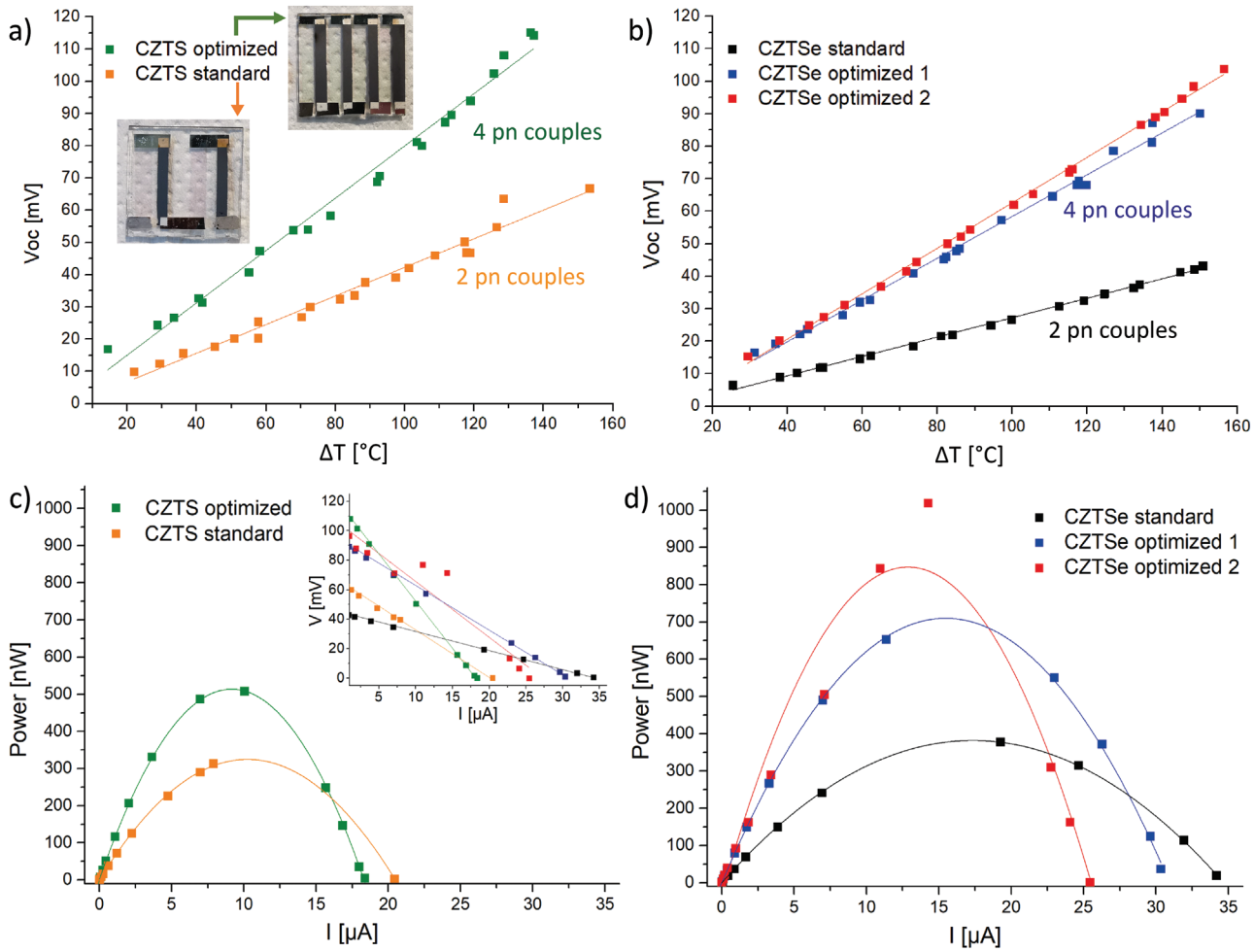

Figure 4. Performance characterization of the TEG devices. Open circuit voltage V_{OC} versus temperature difference ΔT relations for a) CZTS-based and b) CZTSe-based devices. Pictures in (a) show the actual CZTS devices. Current I versus power curves for c) CZTS-based and d) CZTSe-based devices measured with a hot side temperature of 200 °C and a temperature gradient of 150 K. Inset in (c) show the current I versus voltage V curves.

measured before and after a quenching step from a temperature above the transition, to preserve the higher temperature phase. The experimental E_g was found in the order of 1.2 eV, around 200 meV higher than typical literature reports on pristine CZTSe, and no resolvable difference is observed before and after the quenching step (data in Figure S6, Supporting Information). Nevertheless, Raman spectroscopy on quenched samples (in Figure S7, Supporting Information), confirms that Cu–Zn order-disorder phenomena are at place. Therefore, we suggest that the Cu-rich Zn-poor composition might be causing the observed deviation in E_g, and reduced sensitivity of E_g to the increase of Cu–Zn disorder. In Supporting Information, a further verification of electronic properties using a 4-pont probe, and the TEG test setup is presented.

The power factor PF for both CZTS and CZTSe presents an improvement around the transition temperatures, reaching interesting values of 2.4 and 4.4 μW K^{-2} cm^{-1} at 300 °C, respectively. Likely due to the lower Cu–Zn disorder temperature, CZTSe shows a boost in PF in a lower temperature range, suggesting that the material could be comparatively better performing than CZTS in low temperature TE devices.

3.3. Characterization and Performance Analysis of Standard and Optimized Devices

What is required for an efficient device? A TEG figure of merit $ZT = (S_p - S_n)^2 T/RK$ is analogous to the material zT, where the subscripts p and n refer to the p and n-type legs, while R and K are respectively the device electrical resistance and thermal conductance. Therefore, it is necessary to select materials with a high thermopower S, as well as low electrical resistivity to maximize the power output while keeping minimal Joule heat dissipations. A low thermal conductivity is preferred, although in the thin film configuration the thermal transport is typically dominated by the substrate (due to the major difference in thickness). This makes the power factor PF a decisive parameter for the selection of thin film materials.

Thin film thermoelectric devices are fabricated through a sequential deposition of the materials. As illustrated in Figure 1a, first, the CZTS and CZTSe layers are sputtered and a chalcogenization step is applied. The p-type legs are shaped by scratching away the extra film. Masks are then applied to deposit the n-type AZO and the Ag contacts, through sputtering

and thermal deposition, respectively. A picture of the final devices can be seen in Figure 1c. Further details of the fabrication procedure can be found in Section 2.

Raman spectroscopy (Figure 3d) pointed to compositional inhomogeneities in AZO depositions, known to cause differences in electrical resistivity. It was indeed verified that samples cut from the marginal areas of the sputtered batch presented a higher ρ (see data in Supporting Information). To overcome this issue, whenever the ρ of n-type legs was found larger than expected, an additional layer of AZO was sputtered to match the required leg resistance.

As explained in Section 2.4, two configurations were studied: a standard, consisting of constant-width legs (≈3 mm) and 2 p-n couples, and an optimized configuration, featuring 4 p-n couples and a variable width of the legs. The optimization procedure was intended to: i) optimize the usage of the available substrate given the importance, for TEGs, of the generated power per unit area; ii) adjust the relative width of the p and n legs in order to maximize the output performance, considering their respective ratio of electrical to thermal conductance.

For the latter, considering the formulation of a device ZT, the term in which leg dimensional parameters are immediately involved is the denominator $R \times K$. Therefore, a minimization of $R \times K$ is pursued utilizing Equation (1), considering the legs as a series of electrical resistances and as a parallel, together with the SLG substrate, of thermal conductances.

$$ZT = \frac{\left(S_p - S_n\right)^2}{RK} T, \qquad \text{Minimize } RK = \left(\frac{\rho_p}{w_p t_p} + \frac{\rho_n}{w_n t_n}\right) \times \left(\kappa_p w_p t_p + \kappa_n w_n t_n + \kappa_g w_g t_g\right) \tag{1}$$

where t and w stands for thickness and width, while the subscripts p, n, g stand for p-type leg, n-type leg, and SLG substrate, respectively. For practical reasons, the length was designed and considered equal for all the elements, while the thickness was kept fixed to the values known to provide consistent compositional results according to the specific deposition method. Therefore, the relative width of the p over the n legs was chosen as minimization parameter. Further details can be seen in the Supporting Information. Optimized widths were selected as ≈2 mm for n legs and ≈2.5 mm for p legs, for the CZTS-based devices, and ≈3 mm for n legs and ≈1.5 mm for p legs for the CZTSe-based devices.

The device characterization is presented in **Figure 5** and **Table 2**. The open circuit voltage V_{OC} (Figure 5a,b) shows the expected linear trend with increasingly higher applied temperature differences. TEGs in the optimized configuration show a roughly doubled V_{OC}, consistent with the increase of p–n couples from 2 to 4. The voltage generated in open circuit conditions is fundamentally a measure of the cumulative Seebeck coefficient of the TEG. Therefore, CZTS-based devices show higher V_{OC} values than CZTSe-based ones, in accordance with the higher Seebeck coefficient measured for the former.

The current–voltage–power IVP characterization (Figure 5c,d) shows the behavior of the TEGs under an applied variable load, and a constant hot side temperature (T_h = 200 °C of the sample hot side, yielding a $\Delta T \approx 150$ K). Due to the lower electrical resistivity of CZTSe, CZTSe-based devices present a lower internal resistance R_I (Table 2). Obviously, devices in standard configuration (2 p–n couples) present a lower R_I than 4 p–n couple TEGs. The same trends are also visible in the lower slope of the IV plots (inset of Figure 5c) and in the higher values of maximum generated current (Figure 5c,d), for lower R_I devices. The maximum power

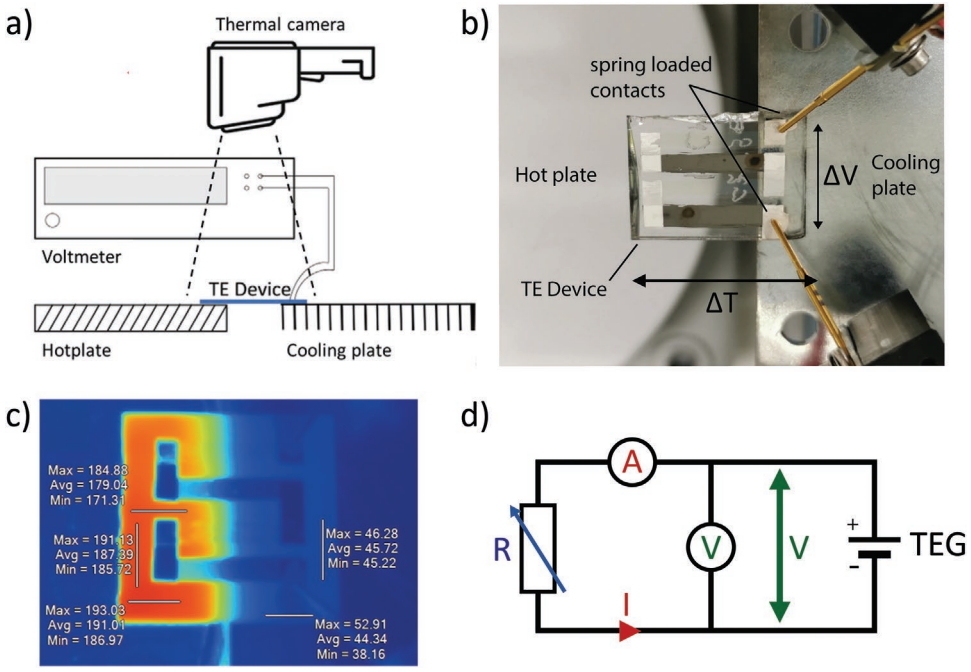

Figure 5. a,b) Sketch and picture of the in-house measuring setup for the V_{OC} versus ΔT plots. c) Thermography of the TEG device under operation. d) Scheme of the equivalent circuit of the setup used to measure the IVP characteristics.

Table 2. Performance characteristics of the CZTS- and CZTSe-based TEGs. Although the design, optimization and measurement setup are conceived for a planar arrangement, the computation of the power per unit cross sectional area (vertical arrangement) shows promising values, pointing to a potential use of the materials for vertical devices.

Device	Internal resistance [kΩ]	Horizontal arrangement				Vertical arrangement	
		Area [cm^2]	Actual area [cm^2]	Power per unit area [$nW\ cm^{-2}$]	Power per unit actual area [$nW\ cm^{-2}$]	Cross-sectional area [cm^2]	Power per unit cross sectional area [$mW\ cm^{-2}$]
CZTS standard	2.7	4.41	2.71	45	117	0.000165	1.922
CZTS optimized	6.64	6.12	3.33	83	152	0.00027	1.875
CZTSe standard	1.23	5.06	2.38	75	158	0.000195	1.928
CZTSe optimized 1	2.9	5.28	2.89	134	246	0.00021	3.385
CZTSe optimized 2	3.79	5.00	3.65	204	279	0.00021	4.849

is obtained at matched conditions, meaning when the device R_I is equal to the load resistance. CZTSe-based TEGs exhibit the highest power, reaching 1 μW for one of the optimized configurations (two specimens are presented to show device to device variability). For the optimized TEGs, the effect of the better utilization of the substrate is visible in the higher power per unit area (Table 2). The optimization of the relative leg width prove effective as well, as the power per unit active area (planar area covered by the legs) is markedly enhanced with respect to the standard configuration. Peak results are obtained with the CZTSe-based devices, with the optimized configuration yielding a maximum power density of almost 280 $nW\ cm^{-2}$. Optimized CZTS reaches a value of 153 $nW\ cm^{-2}$ at matched conditions, almost reaching the peak performance of CZTSe in the standard configuration. It is to be remarked that the quoted power densities are obtained using the planar (not cross sectional) area of the device. Indeed the design, optimization, and measurement setup are conceived for a thin film planar arrangement. Nevertheless, the computed power per unit cross sectional area show promising power densities ranging from ≈2 to almost 5 $mW\ cm^{-2}$. This indicate a potential interest of the device and material coupling for vertical arrangements as well. In the Supporting Information, results of cycling on the *IVP* curves are presented. CZTSe-based devices show a good stability, maintaining over 75% of the original power after 7 cycles. CZTS-based devices show a larger degradation of performance (60% of the original power after 3 cycles). This could be tackled by employing suitable protective coatings. For example, sodium silicate has been demonstrated effective for kesterites.[93]

These results represent the first attempt ever presented to develop a thin film TE generator based on kesterites, as well as an important step towards the actual development of efficient TE devices based on cost-effective, abundant, and sustainable materials.

Table 3 summarizes the performance of thin film TE devices from the literature. To uniform the results, the peak power per unit effective area (planar) and unit temperature difference is considered. In the recent years, several high-performance thin film devices have been presented, mostly achieving power densities in the order of 3–7 $nW\ K^{-1}\ cm^{-2}$.[43,44,94–96] Nevertheless, these results were obtained with devices based on Bi_2Te_3 and Sb_2Te_3 materials. These, albeit high-performing, are known to pose practical issues for a large scale and every-day life application of the thin film TE technology. In fact, Bi and Te are regarded as critical raw materials, while the toxicity of Te and Sb could cause problems for certain applications such as for medical and wearable devices, as well as for the environment. A few attempts of more sustainable thin film TEGs have been reported in the recent literature. Burton et al. developed an SnSe-based generator,[97] while oxide-based devices were proposed by Vieira et al.[98] (SnO_x and ZnO), Ishibe et al.[99] (SnO_2), and Park et al.[85] (Al_2O_3/ZnO superlattice with $Bi_{0.5}Sb_{1.5}Te_3$). Nevertheless, the fabricated TEGs were probably intended more as a proof of concept than end-designed devices, as the peak power densities do not overcome the 0.3 $nW\ K^{-1}\ cm^{-2}$. In this work, we present credible candidates for achieving a more sustainable, eco-friendly, and cheaper thin film TE generation. Indeed, the kesterite-based TEGs reach power densities over 300 to 600% larger than the other sustainable-oriented candidates, with values of ≈1 and ≈1.9 $nW\ K^{-1}\ cm^{-2}$ for the CZTS and CZTSe-based devices, respectively. Furthermore, a drastic cost abatement is achieved as compared to the top-performance Bi_2Te_3 and Sb_2Te_3-based thin film TEGs. As a means for comparison, the cost per unit kg of overall TEG material is calculated based on the standard costs for the raw chemical elements[100,101] and the reported TEG compositions. Very interestingly, by considering the power density per unit cost, the kesterite-based devices result being competitive with most of the top-performing generators.[43,44,94–96] The case of the CZTS-based device is particularly remarkable. In fact, it achieves a power density of 0.183 $nW\ K^{-1}\ cm^{-2}/(€\ kg^{-1})$, fairly in line with top-performance Bi_2Te_3 and Sb_2Te_3 reports mostly ranging from 0.106 to 0.226 $nW\ K^{-1}\ cm^{-2}/(€\ kg^{-1})$, but obtained with a totally non-toxic composition, and with one of the cheapest costs per unit kg. These results represent an important first step towards the realization of cost-effective and sustainable thin film TEGs, unveiling a new class of potentially suitable candidate materials. Further research should be dedicated to the optimization of materials properties by tuning the chemical composition, and of the TEG design, as well as to the exploration of alternative sustainable and low-cost materials.

4. Conclusion

A first realization of thin film TE devices made of cheap, abundant, and sustainable materials is presented, showing interesting thermoelectric conversion efficiencies, compared with devices based on traditional TEs. Kesterite CZTS and CZTSe are utilized as p-type semiconductors, while AZO is employed for the n-type

Table 3. Characteristics, performance, and costs for thin film thermoelectric generators in the recent literature.

Material	Fabrication	*P* max [nW]	Planar area [cm^2]	ΔT [K]	*P* density [$nW/(K\ cm^2)$]	Cost [euro kg^{-1}]	*P* density per unit cost [$(nW\ K\ cm^{-2})/(€\ kg^{-1})$]	Ref.
AZO/CZTS standard	sputtering, 2 pn couples	317	2.71	150	0.78	5.57	0.140	this work
AZO/CZTS optimized	sputtering, 4 pn couples	507	3.33	150	1.02	5.57	0.183	this work
AZO/CZTSe standard	sputtering, 2 pn couples	377	2.38	150	1.06	12.24	0.087	this work
AZO/CZTSe optimized	sputtering, 4 pn couples	1019	3.65	150	1.86	12.24	0.152	this work
Bi_2Te_3/Sb_2Te_3	thermal evaporation,15 pn couples	693	3.75	35	5.28	31.40	0.168	[94]
Bi_2Te_3/Sb_2Te_3	flash evaporation, 7 pn couples	210	2.1	30	3.33	31.40	0.106	[44]
$Bi_2Te_{2.7}Se_{0.3}/Sb_2Te_3$	screen printing, 10 pn couples	2900	8.43	50	6.88	30.48	0.226	[43]
Bi_2Te_3/Sb_2Te_3 degradation operation	thermal evaporation, 20 pn couples	1105	0.7	90	17.54	31.40	0.559	[95]
Bi_2Te_3/Sb_2Te_3 optimal operation	thermal evaporation, 20 pn couples	138	0.7	30	6.57	31.40	0.209	[95]
Bi_2Te_3/Sb_2Te_3	sputtering on polyester paper, 20 pn couples	80	1.6	75	0.67	31.40	0.021	[96]
SnSe	thermal evaporation, 8 p legs	90	3.2	200	0.14	16.62	0.008	[97]
Al_2O_3/ZnO superlattice with $Bi_{0.5}Sb_{1.5}Te_3$	atomic layer deposition, 4 pn couples	1	0.64	80	0.02	17.26	0.001	[85]
SnO_2	pulsed layer deposition, 10 n legs	0.97	0.18	20	0.27	12.41	0.022	[99]
SnO/ZnO	pulsed layer deposition + thermal evaporation, 4 pn couples	1.8	0.64	160	0.02	7.80	0.002	[98]
	toxic/potentially toxic		rare < 0.01 mg kg^{-1}		ideal			

legs. Material characterizations and thermoelectric transport properties are presented, and the electrical resistivity of CZTS and CZTSe show features connected with the Cu–Zn order-disorder transitions. Thin film thermoelectric devices in planar configuration are fabricated through a sequential deposition of the p-type, n-type, and contact materials. A chalcogenization step is applied on the p-type material to reach the desired composition. The devices' planar design is optimized for the sake of a better utilization of the substrate and an increased conversion efficiency. The peak power density is achieved with CZTSe-based devices, reaching values of 279 nW cm^{-2}. A comparison with other sustainable literature candidates shows that the achieved performance is more than one order of magnitude higher, pointing to the chosen materials and design as a promising direction for eco-friendly thin-film devices. Furthermore, a drastic cost abatement of materials is achieved if compared with traditional thermoelectrics. Remarkably, the power density per unit cost achieves values comparable with devices based on Bi_2Te_3 and Sb_2Te_3, but without the issues of material scarcity and toxicity. This represents an important step towards the realization of economically competitive, sustainable, and non-toxic thin-film TE converters, for use in power generation, cooling, and temperature regulation devices.

Supporting Information

Supporting Information is available from the Wiley Online Library or from the author.

Acknowledgements

A.J. thanks the European Social Fund+ for the FI fellowship. The authors would like to acknowledge the help of Dr. Mirco D'Incau, Dr. Narges Ataollahi, and Prof. Della Volpe for the design of the measuring setup, as well as useful discussion with Prof. Dario Narducci. This research has received funding from the Spanish Ministry of Science, Innovation and Universities under the MATER-ONE projects (PID2020-116719RB-C41). Authors from IREC belong to the SEMS (Solar Energy Materials and Systems) Consolidated Research Group of the "Generalitat de Catalunya" (ref. 2017 SGR 862) and are grateful to European Regional Development Funds (ERDF, FEDER Programa Competitivitat de Catalunya 2007–2013). M.G. acknowledges the financial support from Spanish Ministry of Science, Innovation and Universities within the Juan de la Cierva fellowship (IJC2018-038199-I). E.S. acknowledges the ICREA Academia Program.

Open Access Funding provided by Universita degli Studi di Trento within the CRUI-CARE Agreement.

Conflict of Interest

The authors declare no conflict of interest.

Author Contributions

E.I.: Investigation, formal analysis, writing—main draft. J.A.A.: Investigation, formal analysis, writing—review and editing. U.S.: Investigation, formal analysis, writing—review and editing. A.J.A.: Investigation, formal analysis. A.N.G.: Investigation, formal analysis. M.G.: Investigation, formal analysis, writing—review and editing. E.S.: Funding acquisition,

supervision, conceptualization, methodology, writing—review and editing. P.S.: Conceptualization, funding acquisition, supervision, methodology, writing—review and editing.

Data Availability Statement

The data that support the findings of this study are available from the corresponding author upon reasonable request.

Keywords

Al-doped ZnO (AZO), kesterite CZTS CZTSe, thermoelectric generators, thermoelectricity, thin films

Received: February 23, 2022
Revised: May 3, 2022
Published online:

[1] D. M. Rowe, *Modules, Systems, and Applications in Thermoelectrics*, Routledge, Oxfordshire, UK **2012**.
[2] D. M. Rowe, *Thermoelectrics and Its Energy Harvesting*, Routledge, Oxfordshire, UK **2012**.
[3] G. J. Snyder, E. S. Toberer, *Nat. Mater.* **2008**, *7*, 105.
[4] A. Zevalkink, D. M. Smiadak, J. L. Blackburn, A. J. Ferguson, M. L. Chabinyc, O. Delaire, J. Wang, K. Kovnir, J. Martin, L. T. Schelhas, T. D. Sparks, S. D. Kang, M. T. Dylla, G. J. Snyder, B. R. Ortiz, E. S. Toberer, *Appl. Phys. Rev.* **2018**, *5*, 021303.
[5] M. Hong, W. Lyu, Y. Wang, J. Zou, Z. G. Chen, *J. Am. Chem. Soc.* **2020**, *142*, 2672.
[6] G. A. Slack, *The Thermal Conductivity of Nonmetallic Crystals,* Vol. *34,* **1979**.
[7] G. A. Slack, *CRC Handbook of Thermoelectrics*, (ed. M. Rowe), CRC Press, Boca Raton, FL **1995**.
[8] M. Beekman, D. T. Morelli, G. S. Nolas, *Nat. Mater.* **2015**, *14*, 1182.
[9] K. Biswas, J. He, I. D. Blum, C. I. Wu, T. P. Hogan, D. N. Seidman, V. P. Dravid, M. G. Kanatzidis, *Nature* **2012**, *489*, 414.
[10] C. Couder, A. Bourhim, O. I. Lebedev, N. Daneu, F. Appert, J. Juraszek, P. Lemoine, L. Segreto, E. Guilmeau, *Acta Mater.* **2020**, *195*, 229.
[11] S. Sumithra, N. J. Takas, D. K. Misra, W. M. Nolting, P. F. P. Poudeu, K. L. Stokes, *Adv. Energy Mater.* **2011**, *1*, 1141.
[12] M. Hong, M. Hong, K. Zheng, W. Lyv, M. Li, X. Qu, Q. Sun, S. Xu, J. Zou, J. Zou, Z. G. Chen, *Energy Environ. Sci.* **2020**, *13*, 1856.
[13] N. Neophytou, X. Zianni, H. Kosina, S. Frabboni, B. Lorenzi, D. Narducci, *Nanotechnology* **2013**, *24*, 205402.
[14] J. M. O. Zide, D. Vashaee, Z. X. Bian, G. Zeng, J. E. Bowers, A. Shakouri, A. C. Gossard, *Phys. Rev. B* **2006**, *74*, 205335.
[15] Y. Pei, X. Shi, A. Lalonde, H. Wang, L. Chen, G. J. Snyder, *Nature* **2011**, *473*, 66.
[16] Y. Pei, H. Wang, G. J. Snyder, *Adv. Mater.* **2012**, *24*, 6125.
[17] H. Shi, D. Parker, M. H. Du, D. J. Singh, *Phys. Rev. Appl.* **2015**, *3*, 014004.
[18] K. Uchida, S. Takahashi, K. Harii, J. Ieda, W. Koshibae, K. Ando, S. Maekawa, E. Saitoh, *Nature* **2008**, *455*, 778.
[19] M. Hong, W. Lyv, M. Li, S. Xu, Q. Sun, J. Zou, Z. G. Chen, *Joule* **2020**, *4*, 2030.
[20] L. Hicks, M. S. Dresselhaus, *Phys. Rev. B* **1993**, *47*, 12727.
[21] L. Hicks, M. S. Dresselhaus, *Phys. Rev. B* **1993**, *47*, 8.
[22] X. Chen, Z. Zhou, Y. H. Lin, C. Nan, *J. Mater.* **2020**, *6*, 494.
[23] M. S. Dresselhaus, G. Chen, M. Y. Tang, R. Yang, H. Lee, D. Wang, Z. Ren, J. P. Fleurial, P. Gogna, *Adv. Mater.* **2007**, *19*, 1043.
[24] T. C. Harman, P. J. Taylor, D. L. Spears, M. P. Walsh, in *Eighteenth International Conference on Thermoelectrics. Proceedings, ICT'99*, IEEE, Baltimore, MD **1999**, p. 280.
[25] O. Rabin, Y. M. Lin, M. S. Dresselhaus, *Appl. Phys. Lett.* **2001**, *79*, 81.
[26] J. P. Heremans, C. M. Thrush, D. T. Morelli, M. C. Wu, *Phys. Rev. Lett.* **2002**, *88*, 4.
[27] R. Venkatasubramanian, E. Siivola, T. Colpitts, B. O'Quinn, *Nature* **2001**, *413*, 597.
[28] B. Hinterleitner, I. Knapp, M. Poneder, Y. Shi, H. Müller, G. Eguchi, C. Eisenmenger-Sittner, M. Stöger-Pollach, Y. Kakefuda, N. Kawamoto, Q. Guo, T. Baba, T. Mori, S. Ullah, X. Q. Chen, E. Bauer, *Nature* **2019**, *576*, 85.
[29] D. Beretta, N. Neophytou, J. M. Hodges, M. G. Kanatzidis, D. Narducci, M. Martin- Gonzalez, M. Beekman, B. Balke, G. Cerretti, W. Tremel, A. Zevalkink, A. I. Hofmann, C. Müller, B. Dörling, M. Campoy-Quiles, M. Caironi, *Mater. Sci. Eng., R* **2018**, *138*, 100501.
[30] A. Nozariasbmarz, H. Collins, K. Dsouza, M. H. Polash, M. Hosseini, M. Hyland, J. Liu, A. Malhotra, F. M. Ortiz, F. Mohaddes, V. P. Ramesh, Y. Sargolzaeiaval, N. Snouwaert, M. C. Özturk, D. Vashaee, *Appl. Energy* **2020**, *258*, 114069.
[31] T. Sun, B. Zhou, Q. Zheng, L. Wang, W. Jiang, G. J. Snyder, *Nat. Commun.* **2020**, *11*, 572.
[32] M. Goel, M. Thelakkat, *Macromolecules* **2020**, *53*, 3632.
[33] R. J. M. Vullers, R. Van Schaijk, I. Doms, C. Van Hoof, R. Mertens, *Solid State Electron.* **2009**, *53*, 684.
[34] D. Narducci, *J. Phys. Energy* **2019**, *1*, 024001.
[35] I. Petsagkourakis, K. Tybrandt, X. Crispin, I. Ohkubo, N. Satoh, T. Mori, *Sci. Technol. Adv. Mater.* **2018**, *19*, 836.
[36] M. Lindorf, K. A. Mazzio, J. Pflaum, K. Nielsch, W. Brütting, M. Albrecht, *J. Mater. Chem. A* **2020**, *8*, 7495.
[37] Y. Sun, P. Sheng, C. Di, F. Jiao, W. Xu, D. Qiu, D. Zhu, *Adv. Mater.* **2012**, *24*, 932.
[38] T. Park, C. Park, B. Kim, H. Shin, E. Kim, *Energy Environ. Sci.* **2013**, *6*, 788.
[39] G. H. Kim, L. Shao, K. Zhang, K. P. Pipe, *Nat. Mater.* **2013**, *12*, 719.
[40] *Study on the Eu's list of Critical Raw Materials—Critical Raw Materials Factsheets*, European Commission, Brussels **2020**.
[41] *Study on the EU's list of Critical Raw Materials—Non-critical Raw Materials Factsheets*, European Commission, Brussels **2020**.
[42] P. Fan, Z. H. Zheng, Y. Z. Li, Q. Y. Lin, J. T. Luo, G. X. Liang, X. M. Cai, D. P. Zhang, F. Ye, *Appl. Phys. Lett.* **2015**, *106*, 073901.
[43] D. L. Wen, H. T. Deng, X. Liu, G. K. Li, X. R. Zhang, X. S. Zhang, *Microsyst. Nanoeng.* **2020**, *6*, 1.
[44] M. Takashiri, T. Shirakawa, K. Miyazaki, H. Tsukamoto, *Sens. Actuators, A* **2007**, *138*, 329.
[45] Y. Wang, W. Zhu, Y. Deng, B. Fu, P. Zhu, Y. Yu, J. Li, J. Guo, *Nano Energy* **2020**, *73*, 104773.
[46] E. Ojeda-Durán, K. Monfil-Leyva, J. Andrade-Arvizu, I. Becerril-Romero, Y. Sánchez, R. Fonoll-Rubio, M. Guc, Z. J. Li-Kao, J. A. Luna-López, E. Saucedo, *J. Mater. Chem. C* **2021**, *9*, 5356.
[47] J. Andrade-Arvizu, V. Izquierdo-Roca, I. Becerril-Romero, P. Vidal-Fuentes, R. Fonoll-Rubio, Y. Sánchez, M. Placidi, L. Calvo-Barrio, O. Vigil-Galán, E. Saucedo, *ACS Appl. Mater. Interfaces* **2019**, *11*, 32945.
[48] E. Ojeda-Durán, K. Monfil-Leyva, J. Andrade-Arvizu, I. Becerril-Romero, Y. Sánchez, R. Fonoll-Rubio, M. Guc, Z. Jehl, J. A. Luna-López, A. L. Muñoz-Zurita, J. A. D. Hernández-de la Luz, V. Izquierdo-Roca, M. Placidi, E. Saucedo, *Sol. Energy* **2020**, *198*, 696.
[49] S. Giraldo, E. Saucedo, M. Neuschitzer, F. Oliva, M. Placidi, X. Alcobé, V. Izquierdo-Roca, S. Kim, H. Tampo, H. Shibata, A. Pérez-Rodríguez, P. Pistor, *Energy Environ. Sci.* **2018**, *11*, 582.

[50] S. Giraldo, Z. Jehl, M. Placidi, V. Izquierdo-Roca, A. Pérez-Rodríguez, E. Saucedo, *Adv. Mater.* **2019**, *31*, 1806692.
[51] S. K. Wallace, D. B. Mitzi, A. Walsh, *ACS Energy Lett.* **2017**, *2*, 776.
[52] S. Siebentritt, S. Schorr, *Prog. Photovoltaics Res. Appl.* **2012**, *20*, 1114.
[53] N. Ataollahi, F. Bazerla, C. Malerba, A. Chiappini, M. Ferrari, R. Di Maggio, P. Scardi, *Mater. (Basel).* **2019**, *12*, 3320.
[54] U. Syafiq, N. Ataollahi, P. Scardi, *Sol. Energy* **2020**, *196*, 399.
[55] A. Walsh, S. Chen, S. H. Wei, X. G. Gong, *Adv. Energy Mater.* **2012**, *2*, 400.
[56] E. Isotta, S. Pugno, *Nanomaterials* **2019**, *9*, 762.
[57] E. Isotta, B. Mukherjee, C. Fanciulli, N. M. Pugno, P. Scardi, *J. Phys. Chem. C* **2020**, *124*, 7091.
[58] E. Isotta, B. Mukherjee, C. Fanciulli, N. Ataollahi, I. Sergueev, S. Stankov, R. Edla, N. M. Pugno, P. Scardi, *Phys. Rev. Appl.* **2020**, *14*, 064073.
[59] P. Baláž, M. Achimovičová, M. Baláž, K. Chen, O. Dobrozhan, E. Guilmeau, J. Hejtmánek, K. Knížek, L. Kubíčková, P. Levinský, V. Puchý, M. J. Reece, P. Varga, R. Zhang, A. C. S. Sustain, *Chem. Eng.* **2021**, *9*, 2003.
[60] Q. Jiang, H. Yan, Y. Lin, Y. Shen, J. Yang, M. J. Reece, *J. Mater. Chem. A* **2020**, *8*, 10909.
[61] M. L. Liu, F. Q. Huang, L. D. Chen, I. W. Chen, *Appl. Phys. Lett.* **2009**, *94*, 202103.
[62] H. Yang, L. A. Jauregui, G. Zhang, Y. P. Chen, Y. Wu, *Nano Lett.* **2012**, *12*, 540.
[63] D. Chen, Y. Zhao, Y. Chen, B. Wang, Y. Wang, J. Zhou, Z. Liang, *ACS Appl. Mater. Interfaces* **2015**, *7*, 24403.
[64] F. Mehmood, H. Wang, W. Su, M. Khan, T. Huo, T. Chen, G. Chebanova, A. Romanenko, C. Wang, *Inorg. Chem.* **2021**, *60*, 3452.
[65] F. J. Fan, Y. X. Wang, X. J. Liu, L. Wu, S. H. Yu, *Adv. Mater.* **2012**, *24*, 6158.
[66] Y. Dong, H. Wang, G. S. Nolas, *Phys. Status Solidi RRL* **2014**, *8*, 61.
[67] E. Isotta, U. Syafiq, N. Ataollahi, A. Chiappini, C. Malerba, S. Luong, V. Trifiletti, O. Fenwick, N. Pugno, P. Scardi, *Phys. Chem. Chem. Phys.* **2021**, *23*, 13148.
[68] S. Kumar, M. Z. Ansari, N. Khare, *Thin Solid Films* **2018**, *645*, 300.
[69] R. Fonoll-Rubio, J. Andrade-Arvizu, J. Blanco-Portals, I. Becerril-Romero, M. Guc, E. Saucedo, F. Peiró, L. Calvo-Barrio, M. Ritzer, C. S. Schnohr, M. Placidi, S. Estradé, V. Izquierdo-Roca, A. Pérez-Rodríguez, *Energy Environ. Sci.* **2021**, *14*, 507.
[70] J. Andrade-Arvizu, R. Fonoll-Rubio, Y. Sánchez, I. Becerril-Romero, C. Malerba, M. Valentini, L. Calvo-Barrio, V. Izquierdo-Roca, M. Placidi, O. Vigil-Galán, A. Pérez-Rodríguez, E. Saucedo, Z. Jehl Li-Kao, *ACS Appl. Energy Mater.* **2020**, *3*, 10362.
[71] K. C. Nwambaekwe, V. S. John-Denk, S. F. Douman, P. Mathumba, S. T. Yussuf, O. V. Uhuo, P. I. Ekwere, E. I. Iwuoha, *J. Mater. Res. Technol.* **2021**, *12*, 1252.
[72] S. B. Zhang, S. H. Wei, A. Zunger, *Phys. Rev. B – Condens. Matter Mater. Phys.* **2001**, *63*, 075205.
[73] T. Tsubota, M. Ohtaki, K. Eguchi, H. Arai, *J. Mater. Chem.* **1997**, *7*, 85.
[74] J. Loureiro, N. Neves, R. Barros, T. Mateus, R. Santos, S. Filonovich, S. Reparaz, C. M. Sotomayor-Torres, F. Wyczisk, L. Divay, R. Martins, I. Ferreira, *J. Mater. Chem. A* **2014**, *2*, 6649.
[75] L. Choubrac, A. Lafond, C. Guillot-Deudon, Y. Moëlo, S. Jobic, *Inorg. Chem.* **2012**, *51*, 3346.
[76] A. Nateprov, V. C. Kravtsov, G. Gurieva, S. Schorr, *Elektron. Obrab. Mater.* **2013**, *49*, 70.
[77] M. Guc, S. Levcenko, I. V. Bodnar, V. Izquierdo-Roca, X. Fontane, L. V. Volkova, E. Arushanov, A. Pérez-Rodríguez, *Sci. Rep.* **2016**, *6*, 19414.
[78] M. Guc, S. Levcenko, V. Izquierdo-Roca, X. Fontané, E. Arushanov, A. Pérez-Rodríguez, *J. Appl. Phys.* **2013**, *114*, 193514.
[79] H. F. McMurdie, E. H. Evans, M. C. Morris, B. Paretzkin, W. Wong-Ng, L. Ettlineer, C. R. Hubbard, *Powder Diffr.* **1986**, *1*, 64.
[80] C. Insignares-Cuello, X. Fontané, Y. Sánchez-González, M. Placidi, C. Broussillou, J. López-García, E. Saucedo, V. Bermúdez, A. Pérez-Rodríguez, V. Izquierdo-Roca, *Phys. Status Solidi Appl. Mater. Sci.* **2015**, *212*, 56.
[81] M. Guc, F. Tsin, J. Rousset, Y. E. Romanyuk, V. Izquierdo-Roca, A. Pérez-Rodríguez, *J. Phys. Chem. C* **2017**, *121*, 3212.
[82] S. Jantrasee, P. Moontragoon, S. Pinitsoontorn, *J. Semicond.* **2016**, *37*, 092002.
[83] T. Q. Trinh, T. T. Nguyen, D. V. Vu, D. H. Le, *J. Mater. Sci. Mater. Electron.* **2017**, *28*, 236.
[84] N. Ma, J. F. Li, B. P. Zhang, Y. H. Lin, L. R. Ren, G. F. Chen, *J. Phys. Chem. Solids* **2010**, *71*, 1344.
[85] N. W. Park, J. Y. Ahn, T. H. Park, J. H. Lee, W. Y. Lee, K. Cho, Y. G. Yoon, C. J. Choi, J. S. Park, S. K. Lee, *Nanoscale* **2017**, *9*, 7027.
[86] M. Ullah, W. Chunlei, W. Su, D. Liu, A. Zaman, *J. Mater. Sci. Mater. Electron.* **2019**, *30*, 8611.
[87] C. Raju, M. Falmbigl, P. Rogl, X. Yan, E. Bauer, J. Horky, M. Zehetbauer, R. Chandra Mallik, *AIP Adv.* **2013**, *3*, 032106.
[88] J. J. S. Scragg, L. Choubrac, A. Lafond, T. Ericson, C. Platzer-Björkman, *Appl. Phys. Lett.* **2014**, *104*, 041911.
[89] G. Rey, A. Redinger, J. Sendler, T. P. Weiss, M. Thevenin, M. Guennou, B. El Adib, S. Siebentritt, *Appl. Phys. Lett.* **2014**, *105*, 112106.
[90] S. Schorr, G. Gonzalez-Aviles, *Phys. Status Solidi Appl. Mater. Sci.* **2009**, *206*, 1054.
[91] K. Rudisch, A. Davydova, C. Platzer-Björkman, J. Scragg, *J. Appl. Phys.* **2018**, *123*, 161558.
[92] E. Isotta, B. Mukherjee, C. Fanciulli, N. M. Pugno, in *Proceedings TMS,* **2021**, p. 101007.
[93] M. L. Liu, F. Q. Huang, L. D. Chen, I. W. Chen, *Appl. Phys. Lett.* **2009**, *94*, 3.
[94] E. M. F. Vieira, A. L. Pires, J. P. B. Silva, V. H. Magalhães, J. Grilo, F. P. Brito, M. F. Silva, A. M. Pereira, L. M. Goncalves, *ACS Appl. Mater. Interfaces* **2019**, *11*, 38946.
[95] F. Yang, S. Zheng, H. Wang, W. Chu, Y. Dong, *J. Micromech. Microeng.* **2017**, *27*, 55005.
[96] J. P. Rojas, D. Conchouso, A. Arevalo, D. Singh, I. G. Foulds, M. M. Hussain, *Nano Energy* **2017**, *31*, 296.
[97] M. R. Burton, T. Liu, J. McGettrick, S. Mehraban, J. Baker, A. Pockett, T. Watson, O. Fenwick, M. J. Carnie, *Adv. Mater.* **2018**, *30*, 1801357.
[98] E. M. F. Vieira, J. P. B. Silva, K. Veltruská, C. M. Istrate, V. Lenzi, V. Trifiletti, B. Lorenzi, V. Matolín, C. Ghica, L. Marques, O. Fenwick, L. M. Goncalves, *ACS Appl. Mater. Interfaces* **2021**, *13*, 35187.
[99] T. Ishibe, A. Tomeda, Y. Komatsubara, R. Kitaura, M. Uenuma, Y. Uraoka, Y. Yamashita, Y. Nakamura, *Appl. Phys. Lett.* **2021**, *118*, 151601.
[100] Federal Institute for Geosciences and Natural Resources, *Preismonitor (Report)*, **2020**.
[101] CEIS Data, *China Petroleum & Chemical Industry Association: Petrochemical Price: Inorganic Chemical Material*, **2020**.